Geophys. J. Int. (2000) **142,** 000–000

Numerical inversion of deformation caused by pressure sources: application to Mount Etna (Italy)

E. Trasatti, C. Giunchi and N. Piana Agostinetti

Istituto Nazionale di Geofisica e Vulcanologia, 00143 Roma, Italy

(elisa.trasatti@ingv.it)

Accepted 2007 October 26. Received 2007 October 19; in original form 2007 July 27.

SUMMARY

The interpretation of geodetic data in volcanic areas is usually based on analytical deformation models. Although numerical Finite Element modeling allows realistic features such as topography and crustal heterogeneities to be included, the technique is not computationally convenient for solving inverse problems using classical methods. In this paper we develop a general tool to perform inversions of geodetic data by means of 3D FE models. The forward model is a library of numerical displacement solutions, where each entry of the library is the surface displacement due to a single stress component applied to an element of the grid. The final solution is a weighted combination of the six stress components applied to a single element-source. The precomputed forward models are implemented in a global search algorithm, followed by an appraisal of the sampled solutions. After providing extended testing, we apply the method to model the 1993-97 inflation phase at Mt. Etna, documented by GPS and EDM measurements. We consider four different forward libraries, computed in models characterized by homogeneous/heterogeneous medium and flat/topographic free surface. Our results suggest that the elastic heterogeneities of the medium can significantly alter the position of the inferred source, while the topography has minor effect.

Key words: numerical techniques, inversion, geodesy, volcanic structure, Mount Etna.

1 INTRODUCTION

It is often assumed that observed surface displacements in volcanic areas are due to pressure changes in a magma reservoir embedded in the crust at a certain depth. A variety of source mechanisms have been proposed: one of the first models (and probably the most employed) was published by *Mogi* (1958), who studied the response of a homogeneous, isotropic and elastic halfspace to a isotropic dilatation point in axisymmetric geometry. A more general reservoir model is the 3D point-source ellipsoidal cavity studied by *Davis* (1986). The model is composed of a system of double forces of unequal magnitude, located at the ellipsoid center, such that the resulting normal pressure on the inner side of the cavity is uniform. Approximated analytical solutions of the displacement field are provided in a homogeneous and elastic halfspace. This model is characterized by 9 parameters: 3 center coordinates and 6 independent components of the symmetrical stress tensor. Similarly to the Mogi model, its applicability is restricted to cases of source dimension much smaller than depth, because of the point-source approximation. Another anisotropic analytical source was developed by *Yang et al.* (1988): they considered a finite spheroidal source (which is less general than the ellipsoidal cavity, but it has a finite extension). While position and orientation of *Yang et al.* (1988) and *Davis* (1986) sources can be directly constrained by observed surface displacements, source volume computation is possible only by fixing some of the parameters because the analytical formulation contains the factor $P\ V/\mu$, where P is the source pressure, V is the volume source and μ is the elastic rigidity. The trade-off between these parameters is a common problem when elastic rheology is assumed, and independent assumptions must be considered to estimate two of the three parameters and resolve the ambiguity of the source interpretation. Furthermore, in the case of inelastic effects, other rheological parameters must be considered (such as viscosity for Maxwell media, yield stress for plasticity). However, in many cases observed data do not sufficiently constrain these parameters and this is the reason why elastic rheology is most commonly employed in modeling relatively fast deformation episodes.

In recent years, space and terrestrial measurement techniques have largely improved both in precision and in coverage of the Earth, revealing new insights on volcanic deformation processes. The interpretation of this new information may require us to relax the approximation of homo-

geneous and isotropic halfspace upon which the simple deformation models are based. Natural characteristics of volcanic areas such as topography or lateral variations of rheological properties may have great influence on the observed deformation: such complexities can be treated using numerical methods. Models based on finite element (*Williams and Wadge* 1998; *Trasatti et al.* 2003), or boundary element (*Cayol and Cornet* 1998a,b) methods applied to study deformation of different steep volcanoes showed significant effects if the topography is taken into account. *Trasatti et al.* (2005) realized FE models of the Campi Flegrei caldera with plastic rheology, obtaining a deeper source (5 km b.s.l.) with respect to that inferred in the homogeneous elastic medium (3 km b.s.l.), in accordance with petrological and tomographic data. *Bonaccorso et al.* (2005) performed analytical inversions of deformation data at Mt. Etna during 1993-97 with an ellipsoidal pressure source. In the same paper, 3D FE models were developed assuming the same shape and position of the source, but accounting for real topography and elastic heterogeneities of the crustal layers. Significant discrepancies between analytical and numerical models were localized on the volcano edifice, due to the topography and medium characteristics. The inverted ellipsoid parameters were used by *Currenti et al.* (2007) to investigate the effects of topography and elastic layering on the gravity field. Their main finding is that gravity estimates can be biased in terms of mass gain/loss if medium complexities are neglected and homogeneous flat media are used instead.

Few papers address the question of combining forward models taking into account topography or complex sources with nonlinear inversion methods. As an example, *Fukushima et al.* (2005) developed a technique to retrieve complex dike geometries from geodetic data. This approach is based on a combination of a boundary element method with realistic topography and a Neighborhood Algorithm inversion (*Sambridge* 1999a,b). The mixed BEM is used to compute ground displacements assuming a shallow trapezoidal dike source. The method is applied to invert the InSAR data of the February 2000 flank eruption at Piton de la Fournaise, showing that the overestimation of dike parameters can be as high as 20% when topography is not considered. *Masterlark and Lu* (2004) developed a procedure based on standard damped least squares to retrieve amorphous clusters of deformation point-sources. The method consists of a three-dimensional array of potential point-sources (nodes), without imposing a geometrical shape a priori. The intensity of

each node, i.e. its volume change, fluid pressure change or temperature change, is defined through inversion procedures (*Mossop and Segall* 1999; *Vasco et al.* 2002).

This paper has two aims: (1) developing of numerical procedures to perform inversions of geodetic data using FE forward computations; (2) showing the first interpretation of the 1993-1997 inflation phase at Mt. Etna based on a numerical inversion. In Section 2 we describe how we obtain numerical solutions of surface displacements due to general point sources and how these are utilized in the inversion algorithm. In Section 3 we apply the numerical inversion to our test case: the 1993-1997 inflation phase at Mt. Etna, showing the effects on source inference of topography and elastic heterogeneities.

2 FINITE ELEMENT INVERSION

The FE inversion is carried out in two steps. First, a library of precomputed elementary solutions is built. We select a volume of cubic elements inside the volcano that is likely to contain the inflation source. Inside this volume, each finite element is considered to be an elementary source. Surface displacements are computed by loading the element faces with 3 dipoles and 3 double couple forces which are assembled in a stress tensor. This method mimics the behavior of a general point-source and, under specific conditions, the resulting deformation is equivalent to an ellipsoidal cavity with a constant pressure acting on its boundary. Second, the solutions are combined by the Neighbourhood Algorithm to find the optimal position and the 6 independent stress components. The sampled parameter space is then re-sampled to evaluate the Bayesian posterior probability distribution of the parameters.

2.1 FE Source modelling

The source is modelled by applying a stress tensor σ_{ij} to a single finite element (Fig. 1). The superposition principle allows us to compute the total deformation due to a single element-source from the effect of each stress component. The resulting displacement $u_k(x, y, z)$ is a linear combination of the single contributions as follows:

$$u_k(x, y, z) = s_{11}u_k^{11} + s_{22}u_k^{22} + s_{33}u_k^{33} + s_{12}u_k^{12} + s_{23}u_k^{23} + s_{31}u_k^{31} \quad (1)$$

where u_k^{ij} is the computed surface deformation corresponding to σ_{ij} = 1 MPa applied to the element-source and s_{ij} its scaling factor. This follows the analytical procedure by *Davis* (1986) and references therein, who derived approximate analytical solutions of a dilating triaxial ellipsoid as a weighted combination of displacements from 9 double forces located at the ellipsoid center. The eigenvectors of the stress tensor provide the direction cosines of the ellipsoid axes, while the eigenvalues (principal stresses of σ_{ij} identified by σ_a, σ_b and σ_c) are related to ratios c/a and b/a between the semi-axes a, b, c of the ellipsoid ($a \geq b \geq c$). Table 1 of *Davis* (1986) can be used to obtain the ellipsoid axes ratios and internal pressure, given the eigenvalues of σ_{ij}. Conversely, it can be used to determine the stress tensor to be applied to reproduce a specific source, given the axes ratios. Various members of that table have simple representations in terms of their constituent double forces. For $a = b = c$, the principal stresses are all equal $\sigma_a = \sigma_b = \sigma_c$, that is, a center of dilatation. For $a \neq b \neq c$, the principal stresses are inversely related with respect to the axis length $\sigma_c \geq \sigma_b \geq \sigma_a$. In contrast to the analytical formulation by *Davis* (1986), where boundary conditions are satisfied both at the free surface (null tractions) and on the ellipsoidal cavity (constant normal pressure), we only impose the free surface constraint. As a consequence, the stress tensor σ_{ij} is not constrained to represent an ellipsoidal cavity, and may be interpreted, in its general form, to be equivalent to different deformation mechanisms (*Eshelby* 1957; *Yu and Sanday* 1991; *Aki and Richards* 2002).

In this paper we restrict our investigations to a single point-source, but our approach can be generalized to more complex cases. For example, applying stress to more than one element allows us to compute deformation due to a cluster of point-sources (see e.g. *Masterlark and Lu* 2004). Considering the faces of an arbitrary aggregate of elements as the external boundary of a cavity undergoing to a constant overpressure is a further step toward a more realistic source. We emphasize, however, that any generalization of the single point-source requires a significant increase of the parameters that must be justified by the quantity and the quality of available datasets.

We benchmark the displacement solutions for each stress component applied to buried elements of the FE model with the analytical counterpart. At this testing stage, the medium is a homogeneous and elastic halfspace (rigidity μ = 1GPa and Possion ratio ν = 0.25) and the free

surface is flat. The total FE domain extends 140×140×60 km^3 and is composed of about 146,000 8-node isoparametric brick elements. In the source volume the mesh is regular, with cubic elements of side l = 400 m, while the grid spacing progressively increases to 7 km at the boundaries.

We test the homogeneous spherical source (*Mogi* 1958), fixing the overpressure P = 50 MPa and its position in the origin of coordinates ($S_x = S_y = 0$) at depth S_z = -5.5 km. If the volume of the Mogi source $V_{\mathtt{MS}}$ is the same as the FE source $V_{\mathtt{FE}}$ ($V_{\mathtt{MS}} = V_{\mathtt{FE}} = l^3$), the resulting radius is a = 248 m. The Mogi source is equivalent to three orthogonal dipoles: in this case the stress tensor of the FE source is characterized by σ_a = σ_b = σ_c. The dipole intensity is linked to the internal pressure of the Mogi source by $P/\sigma_a = 4/9$. This ratio comes from the relationship between the momentum of the spherical source $M_{\mathtt{MS}} = PV_{\mathtt{MS}}$ and the momentum components of the 3 orthogonal dipoles in the element source $M_{\mathtt{FE}} = \sigma_a V_{\mathtt{FE}}$. If we force the 3 dipoles to reproduce exactly the spherical source, we must compute the normal stress and impose this to be equal to P at distance a from the origin of dipoles (see *Aki and Richards* 2002, Chapter 3 and Problem 8). We find that

$$M_{\mathtt{MS}} = \frac{4\mu}{3(\lambda + 2\mu)} M_{\mathtt{FE}} \tag{2}$$

If $V_{\mathtt{MS}} = V_{\mathtt{FE}}$, then $P = 4\mu\sigma_a/3(\lambda + 2\mu)$, which reduces to $P = 4\sigma_a/9$ if $\lambda = \mu$. In Fig. 2a-c we compare the surface displacements of the two sources: solid line corresponds to the analytical solution and dashed line to the numerical one, obtained by applying the diagonal stress tensor to the element-source. The two solutions are in very good agreement, confirming that the element size and the mesh topology are appropriate to reproduce the analytical model.

As a second test, we consider a shear dislocation with no volume change. The shear stress σ_{xy} = 50 MPa is applied to the faces x = ±200 m and y = ±200 m of the cubic element of the previous test. This force distribution is equivalent either to a vertical left-lateral dislocation oriented along y, or, conversely, to a right-lateral dislocation along x (e.g. *Lay and Wallace* 1995). The analytical equivalent is calculated by the 3D boundary element algorithm 3D-DEF (*Gomberg and Ellis* 1993), based on the dislocation theory by *Okada* (1992). The analytical finite fault has the same extension as the element face, l^2. The equivalence between the two models is obtained by the momentum balance $M_{\mathtt{FE}}$ = $M_{\mathtt{FA}}$, where $M_{\mathtt{FE}}$ = $\sigma_{xy} V_{\mathtt{FE}}$, $M_{\mathtt{FA}}$ = $l^2 \mu \Delta u$, where Δu is the

displacement imposed on the fault. Fig. 2d-f shows the surface displacement components for this test. Also in this case we obtain excellent agreement between the analytical and FE source.

We have shown that the association of a single finite element to a deformation source provides results consistent with analytical solutions. On the one side, the FE-based approach allows us to include heterogeneous media and topography which can be difficult or impossible to treat analytically. On the other side, the following assumptions are necessary to obtain proper results:

(i) source should be deep enough to be considered as a point-source;

(ii) linear elasticity is required to compute the linear combination of the deformation due to each stress component.

Another advantage of this method is that it is not necessary to draw a new FE grid every time that the source position changes since a new model is generated by simply choosing a different element to which the stress conditions are applied. This feature also suggests an easy way to integrate the FE-based computations with a non-linear inversion procedure. Indeed, once the surface displacements due to each potential source are assembled into a library, this set of "Green's functions" constitutes the ensemble of forward models used by the algorithm, described in the next section, to determine the best source parameters for a given dataset.

2.2 Neighborhood Algorithm inversion

We apply a two-stage approach known as Neighbourhood Algorithm (NA) (*Sambridge* 1999a,b) to extract robust estimation of source parameters from deformation data. The first stage consists of a parameter space exploration aimed to preferentially search good data-fitting regions, rather than find a best-fit solution. In the second stage, developed in the framework of Bayesian inference, the previously sampled ensemble is employed to approximate the Posterior Probability Density function (PPD) and to calculate useful proprieties of the ensemble (i.e. mean model, uncertainties). This inversion scheme has been widely tested on different geophysical inverse problems (*Beghein and Trampert* 2004; *Lucente et al.* 2005; *Lohman et al.* 2002; *Fukushima et al.* 2005) and compared to other global Monte Carlo searches (*Sambridge* 1999a; *Piana Agostinetti et al.* 2004). A misfit function is defined to measure the discrepancy between observed data and FE predictions taking

into account different geodetic datasets. Our misfit function is the average of the reduced chi-square calculated for each dataset.

Here, we briefly describe our NA implementation. The deformation source is modeled by a set of 9 parameters $\mathbf{m} = (S_x, S_y, S_z, \sigma_{xx}, \sigma_{yy}, \sigma_{zz}, \sigma_{xy}, \sigma_{yz}, \sigma_{zx},)$ which corresponds to the source position and the 6 stress components, so that we deal with a 9-dimensional model space. The first stage is intended to minimize the misfit between predictions and observations over this parameter space. The a priori conditions on the model parameters are the ranges over which the parameters are defined. NA generates a random sample of n_s models and divides the parameter space into neighbourhoods defined as Voronoi cells. Each of them contains a sampled model and represents the region closer to that model than to the others in the L_2 norm sense. The ensemble of all of the Voronoi cells (Voronoi diagram) forms a coverage of the parameter space, which is employed to direct subsequent samplings. The misfit is computed for each of the n_s models sampled in the parameter space, identifying n_r best performing sources. The search is then continued within the Voronoi cells of the n_r models so identified. This self–adaptive scheme is iterated n_{iter} times to concentrate the search in the most promising region of the models space. The second stage, called *appraisal*, consists of a re-sampling of the PPD surface over the parameter space. According to *Sambridge* (1999b), the PPD surface is approximated using the point-estimation given from each previously sampled model and its Voronoi cell. Therefore, re-sampling the PPD does not need any new forward computation. Bayesian integrals (i.e. mean model and uncertainties) are evaluated at the end of the re-sampling stage.

3 APPLICATION TO THE MOUNT ETNA INFLATION

3.1 Mount Etna Data

Mt. Etna is the largest volcano in Europe and is located at the northeast edge of Sicily. It rises 3320 m a.s.l. and has a basal diameter of about 40 km. The presence of a magma chamber beneath Mt. Etna, which may be responsible for the deformation of the entire edifice, has not been detected within the uppermost 10 km (see *Chiarabba et al.* 2004, for an overview), while a plumbing system whose dimensions are smaller than the resolving power of seismic tomography was suggested

(*Corsaro and Pompilio* 2004). Geodetic data inversions at Mt. Etna have helped to infer some parameters associated to magma reservoirs such as pressure change in a given volume, or shape of the volume for a given pressure change.

As revealed by GPS, Electro-optical Distance Measurements (EDM), leveling and tilt measurements, the December 1991 to March 1993 strong eruption was characterized by very low seismicity and continuous deflation. After the 1991-93 eruption, the seismic activity resumed and the volcano started a new phase of continuous and marked inflation. The inflation process is clearly detected by GPS and EDM networks (Fig. 3a,c). These data show a nearly uniform expansion of each sector monitored by EDM and of the overall volcano edifice (GPS). From the time evolution of the cumulative areal dilatation (defined as the sum of the horizontal strains), it is evident that all the monitored sectors have undergone a nearly constant areal expansion rate from the end of the 1991-93 eruption to 2001 (Fig. 3b). The inflation experienced by Mt. Etna was also detected by more than 400 InSAR images from 1992 to 2001. The time varying surface deformation of the volcano reveals magmatic inflation and radial spreading of the west, south and east flanks of the volcano (*Lundgren et al.* 2004). The inflation phase was ended by a shallow small dike emplacement at the beginning of 1998 (*Bonaccorso and Patanè* 2001), followed by summit eruptions in 1999 and 2001, and by lava fountains during 1998-2001. Together with the radial pattern, a seaward sliding seems to affect the SE flank (Fig. 3a), where displacement vectors increase in amplitude while moving away from the summit area toward the Ionian Sea. Furthermore, some of these stations undergo a negative vertical displacement (MIL and GIA). This evidence has been interpreted as an eastwards sliding associated with a gravitational instability (e.g. *Borgia et al.* 1992).

The observed inflation has been modeled by several analytical sources so far. *Obrizzo et al.* (2004) performed a Bayesian inversion of the leveling data collected between 1994 and 1998, suggesting a simple point-source model located north of the central craters at 4.5 km b.s.l. Attempts to model the inflation by multiple sources were performed by *Lundgren et al.* (2003) and *Puglisi and Bonforte* (2004). The former inverted InSAR data employing a spheroidal source, together with dislocations on two horizontal and vertical planes to decouple the eastern sector of Mt. Etna. The

latter inverted GPS data by means of a Mogi source and two detachment surfaces. The isotropic source was located under the NW flank of Etna, where the maximum dilatation strain was observed. The GPS and EDM datasets used in the present paper have been inverted by *Bonaccorso et al.* (2005), assuming an analytical ellipsoidal source. The retrieved source was located under the summit craters at 4.2 km b.s.l.. *Bonaccorso et al.* (2005) included this source in a FE scheme to estimate effects due to topography and elastic heterogeneities without performing any optimization. However, loading a FE model by a source determined assuming a homogeneous and isotropic half-space may lead to prediction errors (*Masterlark* 2007). Our aim in this paper is to overcome this problem addressing the full inversion of solutions based on FE numerical results with topography and/or heterogeneities.

3.2 FE sources for Mount Etna

We employ the single source model described in Section 2 to interpret the deformation data at Mt. Etna. The forward modeling consists in the selection of a volume inside the FE model where element-sources are allowed, and in the computation of surface displacements for each potential source to which a single stress component is applied. The element-sources are within a regular volume of $8\times8\times8$ km^3 (a total of 8000 element with spacing of 400 m) located below the summit craters of Mt. Etna (Fig. 4). The volume source extent corresponds to the ranges of variations of the source positions S_x, S_y and S_z, listed in Table 1. The volume is centered NW of the summit craters where GPS horizontal data (Fig. 3a) show a divergent pattern. We compute a solution library with 48,000 entries, as the 6 stress components are applied separately to each of the 8000 elements.

A good strategy to understand how topography and elastic heterogeneities affect the inversion predictions is to include each one in separate models and to compare results. We compute four different libraries for each of the following characteristics of the medium: HOmogeneous with Flat free surface (hereinafter model HOF), HEterogeneous with Flat free surface (HEF), HOmogeneous with Topography (HOT), HEterogeneous with Topography (HET) as summarized in Table 2. Mt. Etna topography in HOT and HET is introduced in a restricted area (40×40 km^2) centered on the summit craters (its central part is depicted in Fig. 4), and it extends as a flat surface

beyond this boundary. In models HEF and HET, elastic heterogeneities are computed converting the seismic velocity v_p by *Chiarabba et al.* (2000) to shear modulus using a reference density of 2500 kg/m^3. The density is kept constant since its variations within the medium only slightly affect the elastic computations. The tomography reveals a high velocity volume located SE of the summit craters, that is translated as a 3D high rigidity structure in the numerical model. The values for shear modulus obtained by conversion from seismic velocities are much larger (7.5 to 21.9 GPa) than the value usually employed in homogeneous models (1 GPa), which is usually considered as the effective rigidity of the volcanic edifice. Therefore, the solutions for the stress tensor for the heterogeneous models HEF, HET are scaled by a factor 17, the ratio between the homogeneous rigidity and the mean value of the heterogeneous rigidities. This scale factor was suggested by *Bonaccorso et al.* (2005) to compare results between homogeneous and heterogeneous models by using the same ellipsoidal source. The discrepancy between shear modulus determined by seismic tomography and the effective shear modulus arises from the incoherent nature of the volcanic materials, for which the elastic rheology may not be appropriate.

3.3 Synthetic tests

We consider a known ellipsoidal source centered at $S_x = 496.5$ km, $S_y = 4180.5$ km and $S_z = -4.45$ km (considered from the sea level). The ellipsoid is vertically elongated with dip angle $\delta = 74^\circ$ and characterized by the following stress tensor (MPa):

$$\sigma_{ij} = \begin{pmatrix} 3750 & -625 & 625 \\ -625 & 2500 & 0 \\ 625 & 0 & 1250 \end{pmatrix} \tag{3}$$

For this source we calculate synthetic data at the real GPS and EDM benchmarks (Fig. 3), adding a Gaussian noise with standard deviation equal to data error. For each configuration indicated in Table 2 an inversion is performed: here we show results for HOF but similar results are retrieved for the other models, with misfit values as low as 1. The NA parameters are tuned to: $n_s = n_r = 1000$, $n_{iter} = 70$, computing a total ensemble of 71000 models. For the Bayesian estimation, the PPD surface is re-sampled $9{\cdot}10^5$ times.

Fig. 5 shows the frequency histograms of the NA search and the PPD distributions. The best fit (black dashed line) and mean models (red dashed line) are very similar and really close to the synthetic values (green diamonds), confirming the robustness of the search algorithm and the statistical significance of the results. The source position is retrieved with uncertainties as small as the element size ($\pm$ 200 m) and the stress tensor is determined with residuals lower than 100 MPa or 8% in value. Although the synthetic source is not coincident with any element centroid, the good results attest that the element spacing is an acceptable discretization for our problem. In Fig. 6 we compare data from the synthetic source with results of the mean model (inferred from the parameters PPDs), at GPS and EDM benchmarks. The match is very good since almost all the theoretical values are within data uncertainties.

3.4 Inversion results

We perform four inversions to estimate the best-fit sources for the 1993-1997 inflation data at Mt. Etna, one for each model proposed in Table 2. The NA parameters, fixed during previous synthetic tests, are kept constant, so that only the forward solution libraries change. Fig. 7 depicts results from the PPD calculations performed by Bayesian inference of the NA generated ensembles. The width of the posterior marginal densities is an indicator of the degree of constraint associated to each parameter: the highly peaked patterns make evident that the inverted parameters are well constrained by the available data. The PPDs of σ_{xx}, σ_{yy} for model HEF and σ_{zz} for model HET show double peaking, however this feature can be considered negligible because of the low probability density associated. Major differences among various models are in source locations rather than in stress components, which are less affected by topography and elastic heterogeneities.

Table 3 summarizes the mean models computed from the PPDs, which are representative of the most likely solution at least for single peaked distributions. The stress tensor σ_{ij} has been diagonalized so that the table shows, besides the source locations S_x, S_y and S_z, the principal stresses σ_c, σ_b, σ_a, and the orientation angles (discussed later). If all the models are considered, principal stresses and Euler angles vary over small ranges, meaning that the geodetic dataset puts a strong constraint on source features. A comparison of the performance of each model with respect to the

others can be done looking at the misfit of the best-fit models listed in Table 3. This comparison is legitimate, because the mean models retrieved from Bayesian integration are very close to the best-fit models of the NA search. The misfit reduction is not statistically significant, implying that all the models have the same performance, as also evidenced by the PPDs of Fig. 7.

In Fig. 8 we map the sources together with the seismic velocity anomalies form *Chiarabba et al.* (2000). The source centers are located NW of the summit craters. The differences among the models are mainly due to the heterogeneities characterizing the medium: sources of heterogeneous models HEF, HET have similar S_x and S_y (Fig. 8a). The same applies to homogeneous models HOF, HOT, even if the clustering is less evident. Looking at the N-S and E-W profiles (Fig. 8b, c, respectively), we note that models with topography have a deeper source $S_z \simeq$ -7.3 km with respect to the flat ones $S_z \simeq$ -6.0 km. A reference elevation is used in flat models to take into account the presence of topography, which is typically between sea level and volcano summit (*Cayol and Cornet* 1998a; *Williams and Wadge* 1998). For Mt. Etna we consider the mean elevation of the GPS sites (*Bonaccorso et al.* 2005) corresponding to 1700 m a.s.l. However, we suggest that changing the reference elevation to 400 m a.s.l. would provide a consistent source depth estimation for all the models considered (flat and with topography).

Fig. 9 shows the displacements at GPS stations and the predicted vs. observed EDM elongations from the best HOF and HET models (results for models HEF and HOT are not shown since they are comparable to HOF and HET). The overall pattern of computed horizontal deformation resembles the radial pattern of GPS data (Fig. 9a). The vertical displacements (Fig. 9c) always overestimate the GPS observations, but, at least, follow the data trend. Transversely anisotropic material properties would results in a flatter uplift pattern (*Masterlark* 2007), probably solving the problem of overestimated vertical deformation. However, by considering Fig. 9 with greater detail, we note that all the models fail to predict the negative vertical displacements recorded in the SE side of the volcano, probably caused by subsidence and eastward sliding of the SE sector of Mt. Etna. The EDM elongations (Fig. 9b) are mainly clustered along the diagonal but are characterized by significant scatter. This can be attributed to the fact that EDM networks are located in specific sectors of Mt. Etna that are possibly affected by deformation mechanisms in addition to

the inflation of the whole edifice. The differential motion of the SE flank of the volcano, influencing data fitting, could affect the estimates of source depth and position. Following the approach outlined in this paper, future studies will address the simultaneous effects both of the inflation source and the mechanical decoupling in the SE sector of the volcano.

The stress tensor can be interpreted in terms of an ellipsoidal inflation source (*Davis* 1986): the eigenvectors provide its orientation, while the eigenvalues ratios are related to c/a and b/a. The Euler angles listed in Table 3 identify the ellipsoid orientation: considering that $59^\circ \leq \delta \leq 77^\circ$ and $110^\circ \leq \phi \leq 133^\circ$, the ellipsoidal cavity plunges toward the SE, with high dip angle. The uncertainties of the retrieved principal stresses do not allow us to provide an accurate estimate of the axes ratios but just a range $0.1 < c/a < 0.2$ and $0.1 < b/a < 0.3$. Therefore, the ellipsoid is vertically elongated, with comparable b and c. A graphical sketch of one among the plausible sources is displayed in Fig. 10, where the cavity is characterized by axes ratio $c/a = 0.2$ and $b/a = 0.3$. As far as it concerns the displayed dimensions of a, b and c, they are indicative since there is a trade-off between the volume and overpressure of the ellipsoidal body which does not allow us to determine them unambiguously. However, assuming a source volume $V \simeq 3$ km^3 (e.g. *Bonaccorso et al.* 2005), the overpressure acting inside the source plotted in Fig. 10 is $P \simeq$ 20-30 MPa, in agreement with common values for volcanic modeling. We may mention that the spheroidal source proposed by *Lundgren et al.* (2003) is characterized by an overpressure of $\sim$5 MPa but its volume is larger than our estimate and part of the deformation is accomodated by the detachment surfaces.

Finally, we want to compare our procedure with results by *Bonaccorso et al.* (2005), who inverted the same dataset as ours but using a non-linear least-squares algorithm. *Bonaccorso et al.* (2005) computed the misfit function as a reduced chi-square for all the data, while our misfit function is the average of the reduced chi-square of GPS and EDM dataset. Another difference is that *Bonaccorso et al.* (2005) converted the GPS horizontal data into relative elongations taking into account the vertical components separately. They retrieved the following source: S_x = 500.7 $\pm$0.3 km, S_y = 4178.0$\pm$0.3 km and S_z = -4.2$\pm$0.3 km. Our inversion, based on model HOF with the same data and misfit function as in *Bonaccorso et al.* (2005), suggests a source located at S_x

= 500.5$\pm$0.2 km, S_y = 4177.6$\pm$0.2 km and S_z = -5.2$\pm$0.2 km. It is interesting to note that the two inversions, performed with different techniques, provide the same source (only S_z is slightly different). The shape and orientation of the analytical and numerical inverted ellipsoids are very similar, being vertically elongated and dipping SE in both cases.

4 CONCLUSIONS

In this paper we address the problem of inverting geodetic data in complex media with a general source. Numerical techniques allow us to include realistic characteristics such as topography and elastic discontinuities, but are less versatile for implementation in inversion techniques. We develop a general, nonlinear procedure to perform inversions of different geodetic datasets by FE forward models. The main advantage of this technique is that the source shape is not fixed a priori, since the retrieved stress tensor may represent a sill, a sphere, an ellipsoid, a fault, etc. This is a first step toward the generalization of volcanic sources, because the shape of the source is a result of the inversion. Furthermore, the direct search method (*Sambridge* 1999a) is followed by the appraisal stage (*Sambridge* 1999b), to infer statistical properties of the parameter space. This step, based on Bayesian inference, allows us to extract information (i.e. PPD distributions) from a generated ensemble, rather than selecting a single set of best-fit parameters.

A further step is required to interpret the stress tensor in terms of equivalence of force systems, addressing a geometrical shape to the point-source. However, the interpretation may not be unique if the geometry is complex and/or the uncertainties associated with the stress tensor are large. In the case of Mt. Etna, the computed PPDs for the stress tensor are very narrow and single peaked, for all models considered, indicating that the parameters are well defined. All the inversions agree in identifying an elongated source, dipping SE and located under the NW flank. However, the uncertainties associated with the PPDs of the stress tensor, even if lower than 10-15% of their peak value, do not allow us to determine the ellipsoid axes uniquely. We are able to indicate ranges of variation of axes ratios: $0.1 < c/a < 0.2$ and $0.1 < b/a < 0.3$. It means that choosing values for a, b and c within these ranges does not make any significant difference in the model predictions.

Our numerical computations clearly show that source position predicted by the topographic,

heterogeneous media HEF, HOT, HET can be significantly different from the simple homogeneous, flat elastic case HOF. Indeed, despite the similar shape, the ellipsoid position varies depending on the characteristics of the medium (see Fig. 8). In particular, the source centers are modified by the presence of heterogeneities. Models HEF and HET (heterogeneous flat and heterogeneous with topography, respectively) have similar S_x and S_y components; the same applies to models HOF and HOT (homogeneous flat and homogeneous with topography, respectively). The seismic tomographic images by *Chiarabba et al.* (2000), displayed in Fig. 8, show a high velocity body laying below the summit craters, translated in high rigidity in the FE model. The presence of this high rigidity volume causes smaller displacements, so that higher stresses or a closer source are needed in order to obtain the same deformation and to contrast the reduction. Therefore, the best-fit sources in the heterogeneous models are shifted toward this volume with respect to the homogeneous models, to accommodate the loss of deformation. Alternatively, the topography has influence on the source depth. The sources inferred within topographic media (HOT, HET) are deeper with respect to the flat ones (HOF, HEF). The reference elevation (i.e. the equivalent of the free surface in flat models) is very important, and should be chosen to allow consistent estimations of depths between different models.

In agreement with others studies (e.g. *Masterlark* 2007), we show that the volcanic structure has a larger impact than topography on the source position inference. Unfortunately, the internal structure itself is usually poorly known for most volcanic areas. Our findings suggest that source inversion procedures should be always integrated with all the available information, i.e. different datasets, topography, rigidity contrasts, tomographic and petrological studies. For example, tomographic imaging of v_p/v_s and Q factor (e.g. *De Gori et al.* 2005) can be used to constrain volumes of melt or highly fractured materials, giving an indication of the reliability of the elastic assumption in some areas. Conversely, the presence of heterogeneities and/or topography does not play a significant role in amplifying the deformation in the SE sector of Mt. Etna, which is certainly due to other mechanisms than the inflation of an internal source. Indeed, none of the inferred sources is able to predict the enhanced horizontal and negative vertical displacements recorded in this area. For this reason, we are aware that it is likely that our results about source position and depth are

biased by the fact that we employ a single pressure source. For example, there is a systematic under prediction of displacement at the summit of Mt. Etna, probably because the inversion tries to fit simultaneously the more distant vectors affected by flank instability. This could impact on the inference of the source depth because a deeper source is more effective in enhancing horizontal motions at greater radial distance. This could reconcile the deeper sources (about 7 km b.s.l.) retrieved by models HET and HOT with other published results (e.g. *Lundgren et al.* 2003; *Bonaccorso et al.* 2005). The effects of a double/multiple source, including the additional deformation caused by a sliding of the SE flank of Mt. Etna will be taken into account in a following paper.

ACKNOWLEDGMENTS

Many thanks are due to Maurizio Bonafede, Alessandro Bonaccorso and Giuseppe Puglisi for helpful discussions and hints. Comments from the editor John Beavan, Paul Lundgren and an anonymous reviewer greatly improved this paper. This study was funded by Italian Civil Protection INGV-DPC V3-6 Etna Project.

REFERENCES

Aki, K., and P. G. Richards (2002), *Quantitative seismology, Second Edition*, 700 pp., University Science Books, Sausalito, CA.

Beghein, C., and J. Trampert (2004), Probability density functions for radial anisotropy from fundamental mode surface wave data and the Neighbourhood Algorithm, *Geophys. J. Int., 157,* 1163–1174, doi: 10.1111/j.1365-246X.2004.02235.x.

Bonaccorso, A., and D. Patanè (2001), Shear response to an intrusive episode at Mt.Etna volcano (January 1998) inferred through seismic and tilt data, *Tectonophysics*, *334*, 61–75.

Bonaccorso, A., S. Cianetti, C. Giunchi, E. Trasatti, M. Bonafede, and E. Boschi (2005), Analytical and 3D numerical modeling of Mt. Etna (Italy) volcano inflation, *Geophys. J. Int., 163,* 852–862, doi: 10.1111/j.1365-246X.2005.027777.x.

Borgia, A., L. Ferrari, and G. Pasquarè (1992), Importance of gravitational spreading in the tectonic and volcanic evolution of Mt.Etna, *Nature, 357,* 231–234.

Cayol, V., and F. H. Cornet (1998a), Effects of topography on the interpretation of the deformation field of prominent volcanoes – Application to Etna, *Geophys. Res. Lett., 25,* 1979–1982.

Cayol, V., and F. H. Cornet (1998b), Three-dimensional modelling of the 1983-1984 eruption at Piton de la Fournaise Volcano, Réunion Island, *J. Geophys. Res.*, *103*, 18,025–18,037.

Chiarabba, C., A. Amato, E. Boschi, and F. Barberi (2000), Recent seismicity and tomographic modelling of the Mount Etna plumbing system, *J. Geophys. Res.*, *105*, 10,923–10,938.

Chiarabba, C., P. De Gori, and D. Patanè (2004), The Mt.Etna plumbing system: the contribution of seismic tomography, *Mount Etna Volcano Laboratory*, *143*, edited by A. Bonaccorso and S. Calvari and M. Coltelli and C. D. Negro and S. Falsaperla, American Geophysical Union Monography Series, 384 pp.

Corsaro, R., and M. Pompilio (2004), Buoyancy-controlled eruption at Mt.Etna, *Terra Nova*, *16*, 16–22.

Currenti, G., C. Del Negro, and G. Ganci (2007), Modelling of ground deformation and gravity fields using finite element method: an application to Etna volcano, *Geophys. J. Int.*, *169*, 775–786, doi: 10.1111/j.1365-246X.2007.03380.x.

Davis, P. M. (1986), Surface deformation due to inflation of an arbitrarily oriented triaxial ellipsoidal cavity in an elastic half-space, with referece to Kilauea volcano, Hawaii, *J. Geophys. Res.*, *91*, 7429–7438.

De Gori, P., C. Chiarabba, and D. Patanè (2005), Q_p structure of Mt.Etna: constraints for the physics of the plumbing system, *J. Geophys. Res.*

Eshelby, J. D. (1957), The determination of the elastic field of an ellipsoidal inclusion, and related problems, *Proc. R. Soc. London, Ser. A*, *241*, 376–396.

Fukushima, Y., V. Cayol, and P. Durand (2005), Finding realistic dike models from the interferometric synthetic aperture radar data: the February 2000 eruption at Piton de la Fournaise, *J. Geophys. Res.*, *110*, doi:10.1029/2004JB003268.

Gomberg, J. S., and M. Ellis (1993), 3D-DEF: a user's manual (a three-dimensional, boundary element modeling program), *Tech. Rep. OF 93-0547*, U.S. Geological Survey.

Lay, T., and T. C. Wallace (1995), *Modern global seismology*, 521 pp., Academic press, San Diego, California.

Lohman, R. B., M. Simons, and B. Savage (2002), Location and mechanism of the Little Skull Mountain earthquake as constrained by satellite radar interferometry and seismic waveform modeling, *J. Geophys. Res.*, *107*, doi:10.1029/2001JB000627.

Lucente, F. P., N. Piana Agostinetti, M. Moro, G. Selvaggi, and M. Di Bona (2005), Possible fault plane in a seismic gap area of the southern Apennines (Italy) revealed by receiver function analysis, *J. Geophys. Res.*, *110*, doi:10.1029/2004JB003187.

Lundgren, P., P. Berardino, M. Coltelli, G. Fornaro, R. Lanari, G. Puglisi, E. Santosti, and M. Tesauro (2003), Coupled magma chamber inflation and sector collapse slip observed with synthetic aperure radar interferometry on Mt.Etna volcano, *J. Geophys. Res.*, *108*, doi:10.1029/2001JB000657.

Lundgren, P., F. Casu, M. Manzo, A. Pepe, P. Berardino, E. Sansosti, and R. Lanari (2004), Gravity and magma induced spreading of Mt. Etna volcano revealed by satellite radar interferometry, *Geophys. Res.*

Lett., *31*, doi:10.1029/2003GL018736.

Masterlark, T. (2007), Magma intrusion and deformation predictions: sensitivities to the Mogi assumptions, *J. Geophys. Res.*, *112*, doi:10.1029/2006JB004860.

Masterlark, T., and Z. Lu (2004), Transient volcano deformation source imaged with interferome tric synthetic aperture radar: application to Seguam Island, Alaska, *J. Geophys. Res.*, *109*, doi: 10.1029/2003JB002568.

Mogi, K. (1958), Relation between the eruptions of various volcanoes and deformations of the ground surfaces around them, *Bull. Earth. Res. Inst.*, *36*, 99–134.

Mossop, A., and P. Segall (1999), Volum strain within the Geiser geothermal field, *J. Geophys. Res.*, *104*, 29,113–29,131.

Obrizzo, F., F. Pingue, C. Troise, and G. De Natale (2004), Bayesian inversion of 1994-98 vertical displacements at Mt.Etna; evidence for magma intrusion, *Geophys. J. Int.*, *157*, 935–946.

Okada, Y. (1992), Internal deformation due to shear and tensile faults in a halfspace, *Bull. Seism. Soc. Am.*, *82*, 1018–1040.

Piana Agostinetti, N., G. Spada, and S. Cianetti (2004), Mantle viscosity inference: a comparison between simulated annealing and neighbourhood algorithm inversion methods, *Geophys. J. Int.*, *157*, 890–900, doi:10.1111/j.1365-246X.2004.02237.x.

Puglisi, G., and A. Bonforte (2004), Dynamics of Mount Etna Volcano inferred from static and kinematic GPS measurements, *J. Geophys. Res.*, *109*, B11 404, doi:10.1029/2003JB002878.

Sambridge, M. (1999a), Geophysical inversion with a Neighborhood Algorithm – I. Searching a parameter space, *Geophys. J. Int.*, *138*, 479–494.

Sambridge, M. (1999b), Geophysical inversion with a Neighborhood Algorithm – II. Appraising the ensemble, *Geophys. J. Int.*, *138*, 727–746.

Trasatti, E., C. Giunchi, and M. Bonafede (2003), Effects of topography and rheological layering on ground deformation in volcanic regions, *J. Volcanol. Geotherm. Res.*, *122*, 89–110.

Trasatti, E., C. Giunchi, and M. Bonafede (2005), Structural and rheological constraints on source depth and overpressure estimates at the Campi Flegrei Caldera, Italy, *J. Volcanol. Geotherm. Res.*, *144*, 105–118.

Vasco, D. W., C. Wicks, K. Karasaki, and O. Marques (2002), Geodetic imaging: reservoir monitoring using satellite interferometry, *Geophys. J. Int.*, *149*, 555–571.

Williams, C. A., and G. Wadge (1998), The effects of topography on magma deformation models: application to Mt.Etna and radar interferometry, *Geophys. Res. Lett.*, *25*, 1549–1552.

Yang, X., P. M. Davis, and J. H. Dieterich (1988), Deformation from inflation of a dipping finite prolate spheroid in an elastic halfspace as a model for volcanic stressing, *J. Geophys. Res.*, *93*, 4249–4257.

Yu, H. Y., and S. C. Sanday (1991), Elastic field in joined semi-infinite solids with an inclusion, *Proc. R.*

Soc. London, Ser. A, 434, 521–530.

Parameter	Min Value	Max Value
S_x (km)	495.2	503.2
S_y (km)	4175.8	4183.8
S_z (km)	-9.2	-1.2
σ_{xx} (MPa)	0	5000
σ_{yy} (MPa)	0	5000
σ_{zz} (MPa)	0	5000
σ_{xy} (MPa)	-1250	1250
σ_{yz} (MPa)	-1250	1250
σ_{zx} (MPa)	-1250	1250

Table 1. Parameters ranges used in the inversions. S_x and S_y are the source position in UTM reference; S_z is the depth referred to the sea level. The source centers are contained in a volume of $8\times8\times8$ km^3. The stress tensor associated to the element-sources is σ_{ij}.

Model	Topography	Elastic rheology
HOF	no	homogeneous
HEF	no	heterogeneous
HOT	yes	homogeneous
HET	yes	heterogeneous

Table 2. Characteristics of the models. The inversions are performed in the homogeneous/heterogeneous medium, with/without the real topography of Mt. Etna.

Model	Misfit	S_x (km)	S_y (km)	S_z (km)	σ_c (MPa)	σ_b (MPa)	σ_a (MPa)	δ (deg)	ϕ (deg)	ψ (deg)
HOF	9.5	498.2	4180.8	-6.0	4716	3354	2405	67	111	-8
HEF	8.9	499.0	4179.5	-6.0	4739	3708	2727	77	133	-1
HOT	10.0	496.9	4180.7	-7.4	4970	3181	2340	59	110	-13
HET	9.8	498.5	4179.8	-7.3	5048	3671	2800	62	120	-3

Table 3. Results of the Neighborhood Algorithm inversion of the 1993-97 GPS and EDM data for models HOF (homogeneous, flat), HEF (heterogeneous, flat), HOT (homogeneous, topography), HET (heterogeneous, topography). The parameters σ_c, σ_b, σ_a are the principal stresses computed from the inverted stress tensor σ_{ij}. The last 3 columns are the Euler angles of the principal stresses: δ indicates the dip of σ_a (positive from the horizontal plane); ϕ represents the orientation of its surface projection measured counterclockwise from x (East); ψ identifies the rotation of σ_c around σ_a.

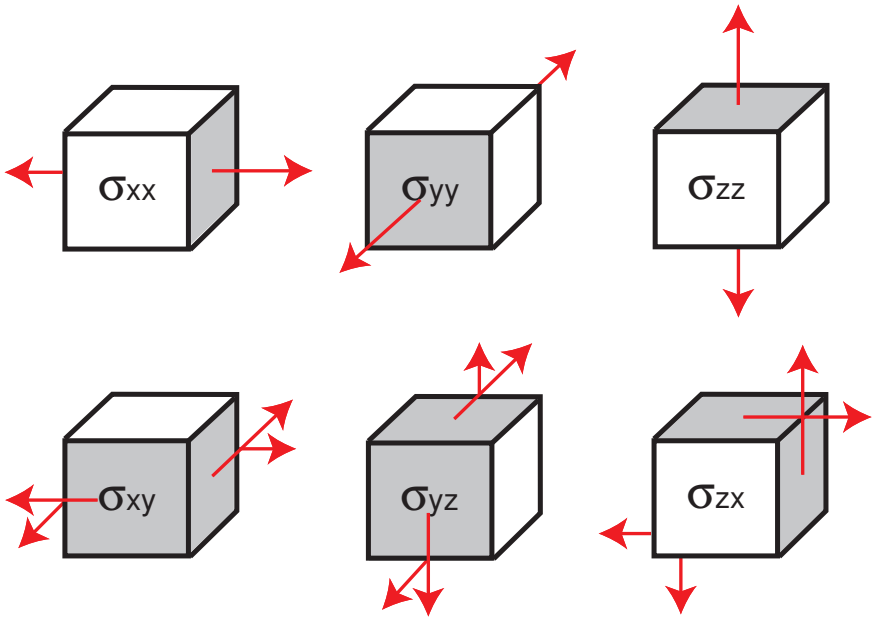

Figure 1. Basic point-source mechanisms consisting in dipoles and double couples. These forces are applied as a stress tensor to a finite element of the grid.

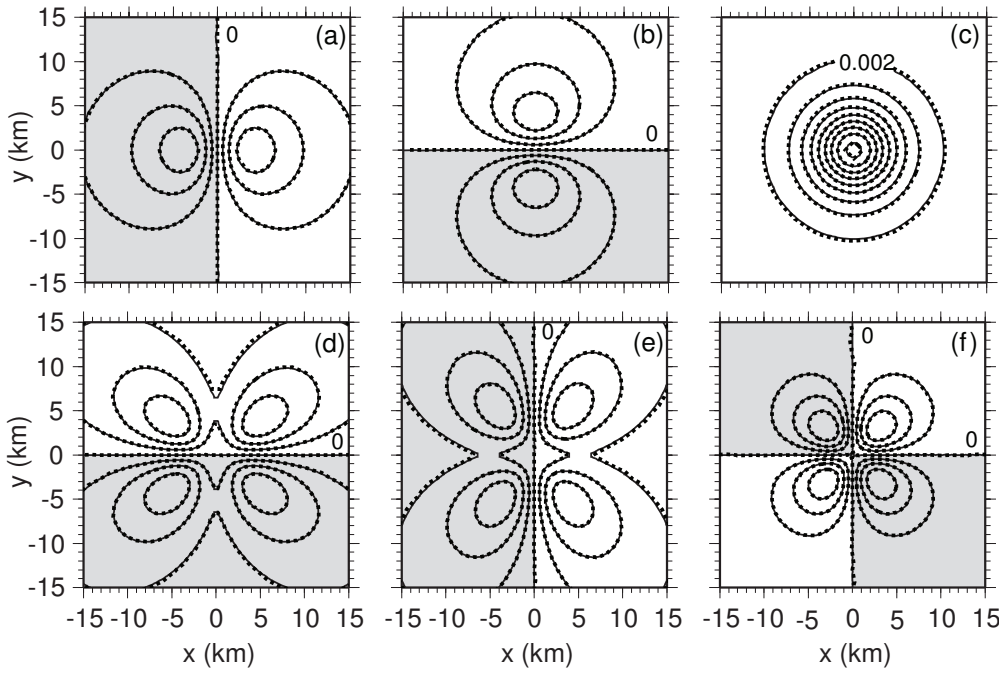

Figure 2. Comparison between analytical and numerical solutions for simple mechanisms. Panels (a, b, c): surface displacements u_x, u_y and u_z, respectively, generated by three orthogonal dipoles realized by FE, and the analytical solution of the isotropic source (*Mogi* 1958); contour spacing is 0.002 m. Panels (d, e, f): surface displacements u_x, u_y and u_z, respectively, due to a vertical left-lateral N-S oriented fault; contour spacing is 0.001 m. The solid line represents the analytical displacement, the dashed line the FE solution. The gray shaded sectors are characterized by negative values.

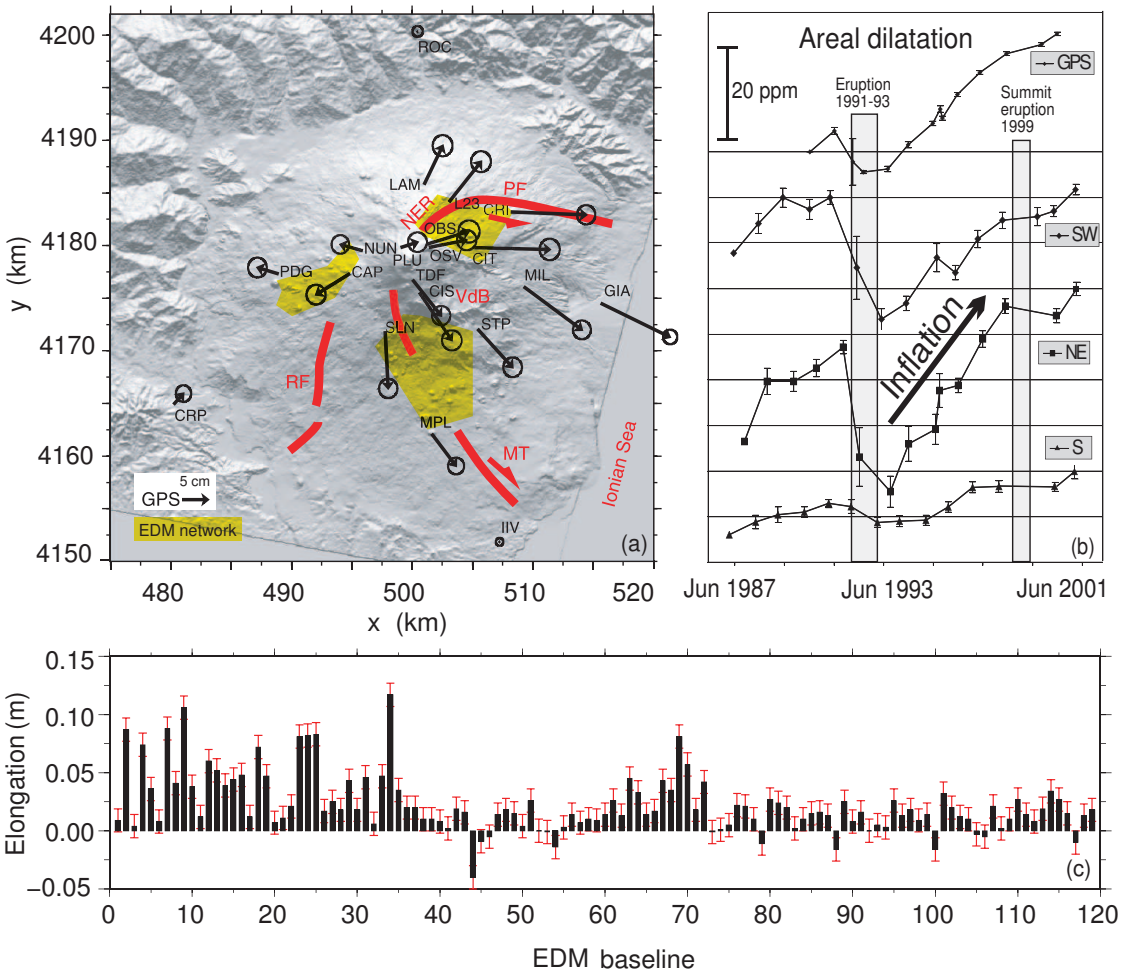

Figure 3. Mt. Etna geodetic data. (a) GPS horizontal displacements recorded at Mt. Etna from 1993 to 1997. For each GPS station (20 in total), name and ellipse error are also shown. The yellow patches show areas covered by the three sections of the EDM network. The red lines mark the major surface fault systems bordering the eastern and southern sectors of the volcano (NER = North East Rift, PF = Pernicana fault, MT = Mascalucia Trecastagni fault; RF = Ragalna fault; VdB = Valle del Bove). (b) Cumulative planar areal dilatation of Mt. Etna from 1987 to 2001, computed for the networks shown in panel (a). A fairly continuous expansion affected the volcanic edifice starting from 1993 to the 2001 flank eruption. (c) 119 EDM elongations from 1993 to 1997 computed in the areas indicated in (a). Data error is indicated in red.

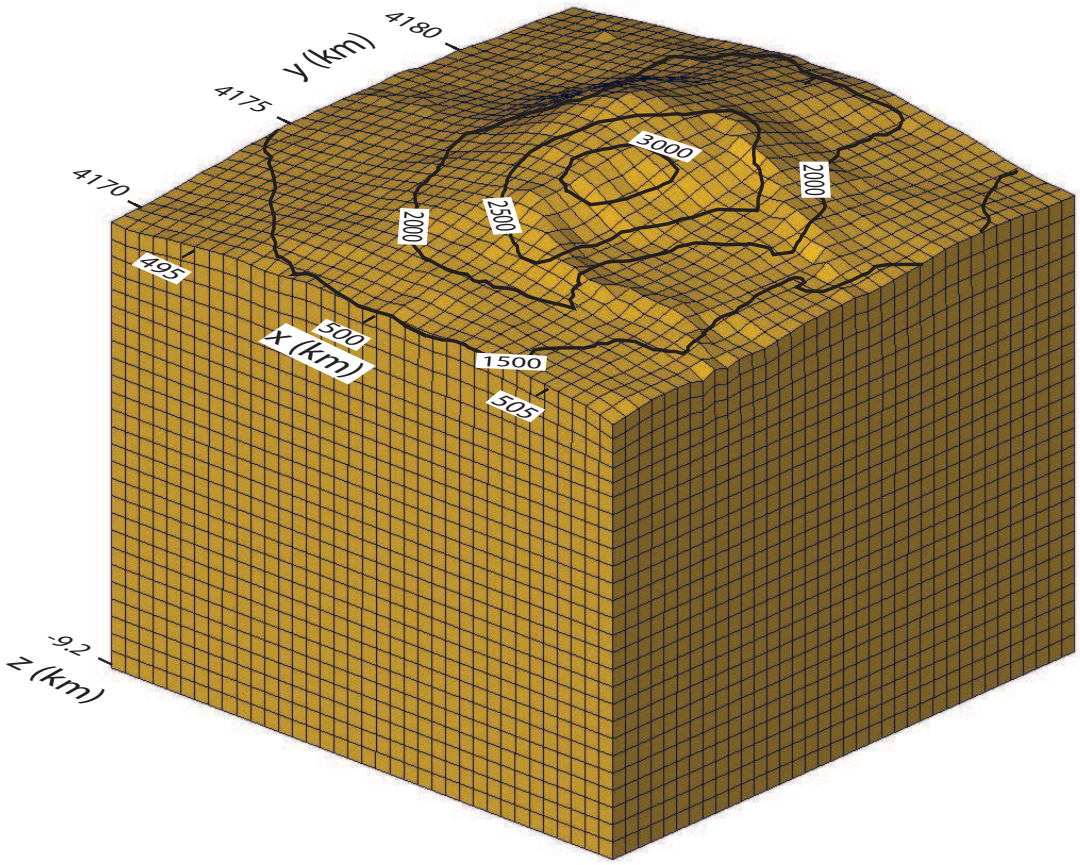

Figure 4. FE model of Mt. Etna. The entire FE domain extends up to $140\times140\times60$ km^3, while the topography is introduced in a restricted area of 40×40 km^2. The very central part of the model is characterized by cubic elements, as shown. The volume of allowed element-sources is contained within this portion of the mesh. The superimposed contour is the elevation in meters of Mt. Etna. The view is from SE.

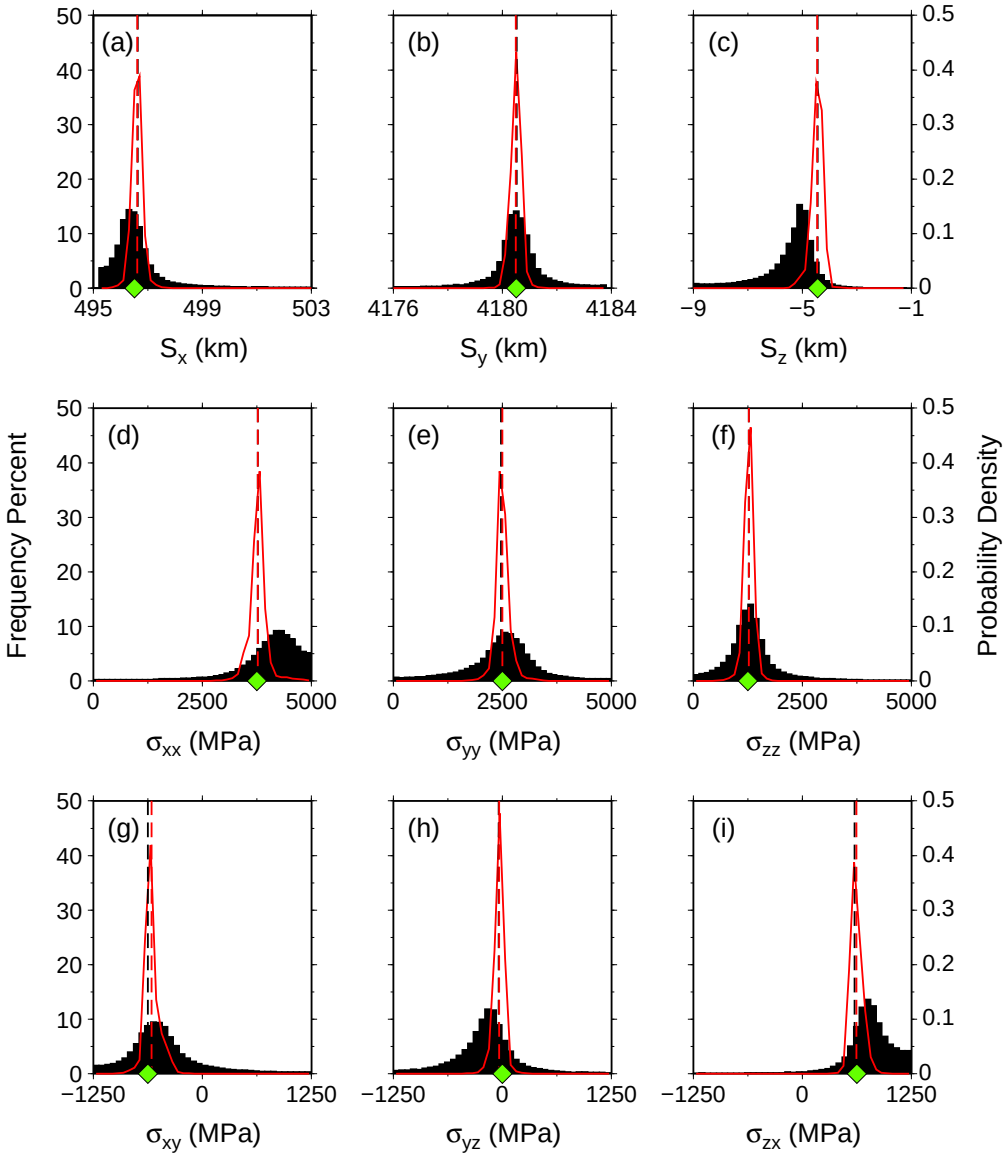

Figure 5. Frequency histograms of the best-fit models and Posterior Probability Density distributions (computed by means of Bayesian inference) of the synthetic test for an ellipsoidal source in a flat, homogeneous medium. The synthetic values are represented with the green diamond. The black histograms are the NA sampling of parameters in the model space, where the black dashed line is the best-fit model. The PPDs are represented in red, where the red dashed line is the mean model. The misfit is as low as 1. Similar results are obtained for models with heterogeneities and/or topography.

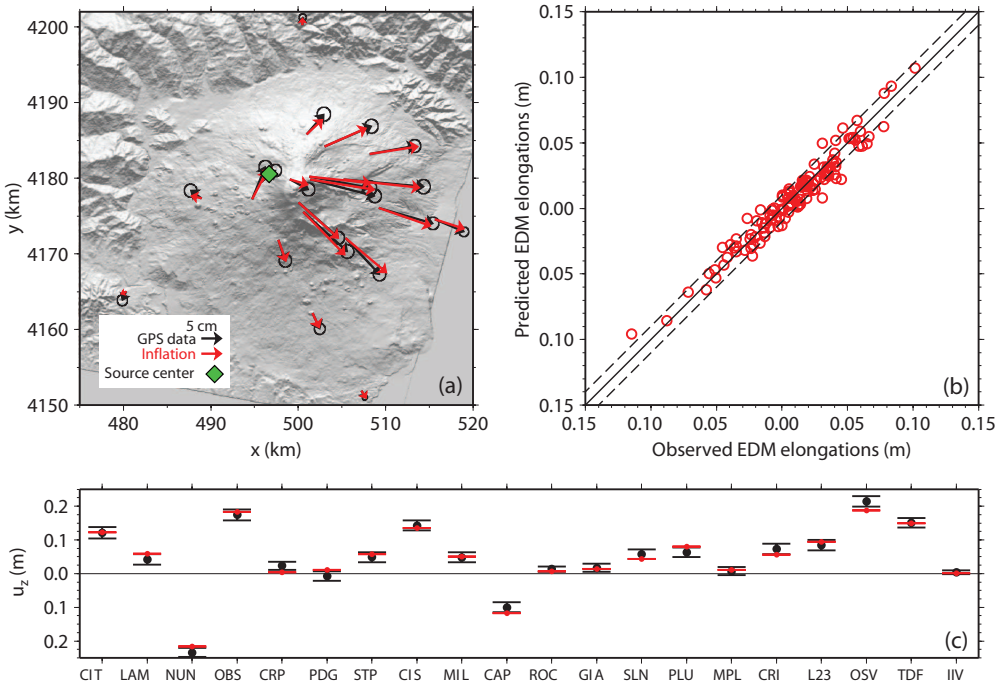

Figure 6. Comparison between synthetic data and predictions for: (a) GPS horizontal data; (b) EDM elongations; (c) vertical GPS displacements.

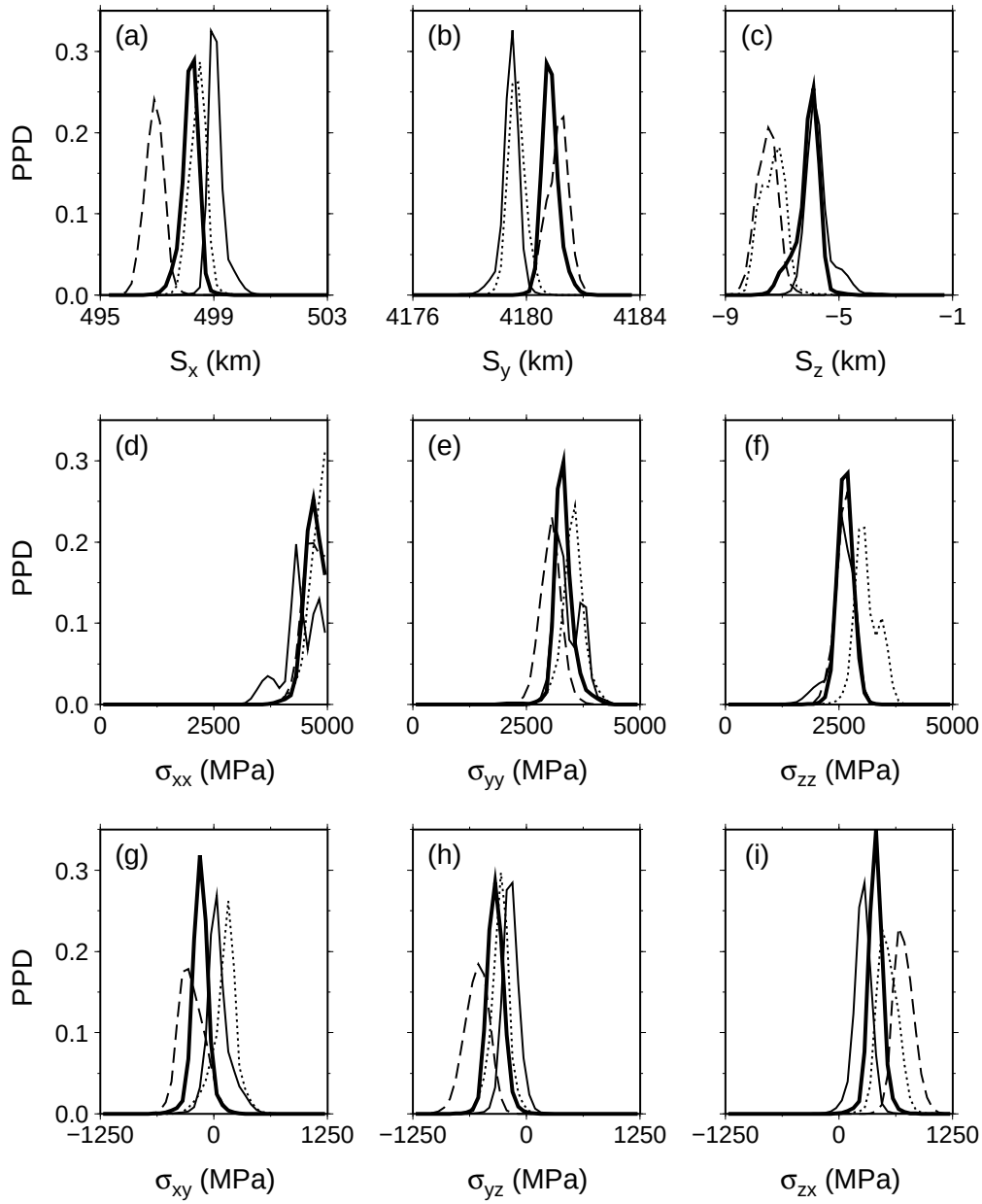

Figure 7. PPD distributions calculated on the ensemble generated by NA. The inversion of the GPS and EDM datasets is performed for all the models of Table 2: HOF, thick solid line; HEF, thin solid line; HOT, dashed line; HET, dotted line. The mean values of these distributions are indicated in Table 3.

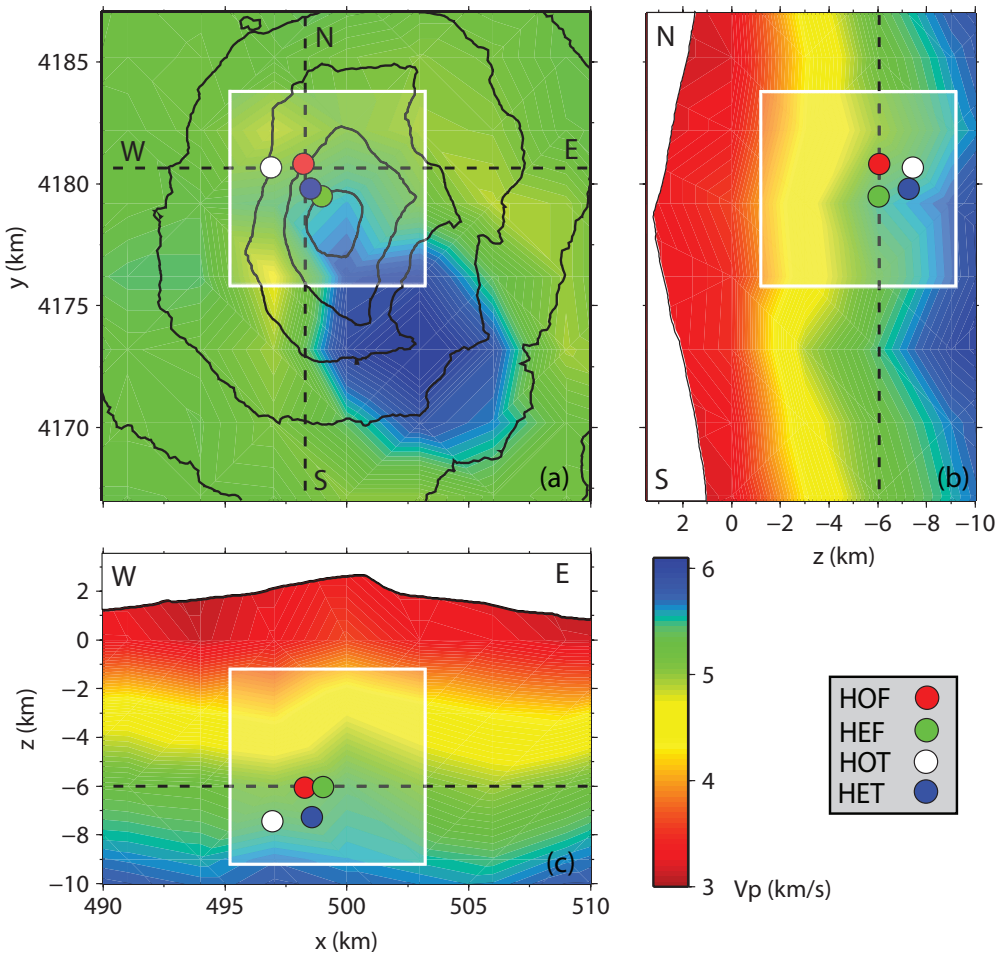

Figure 8. Best-fit source locations for the inverted models. Velocity anomalies (from *Chiarabba et al.* 2000) viewed from (a) top, (b) N-S and (c) E-W sections are also shown. Dashed lines indicate the section planes; white squares are the volume where the element-sources are allowed.

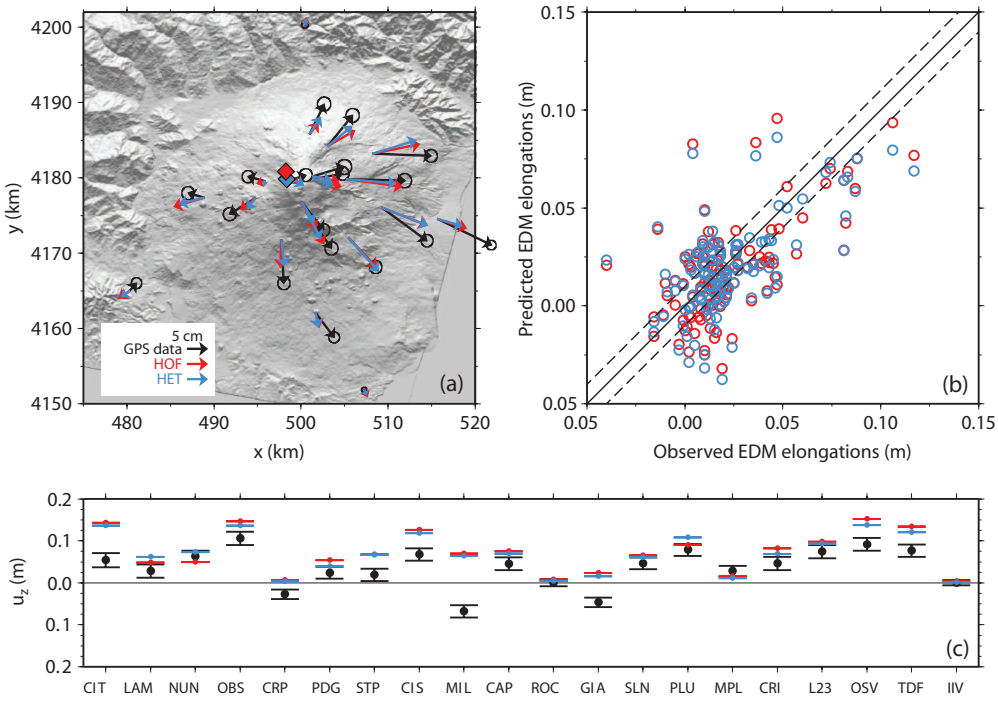

Figure 9. Experimental and computed data, resulting from source inversion in the flat and homogeneous model (HOF) and the heterogeneous and topographic model (HET). Comparison with: (a) GPS horizontal data; (b) EDM elongations; (c) GPS vertical data. Source positions for each model are indicated with red and blue diamonds.

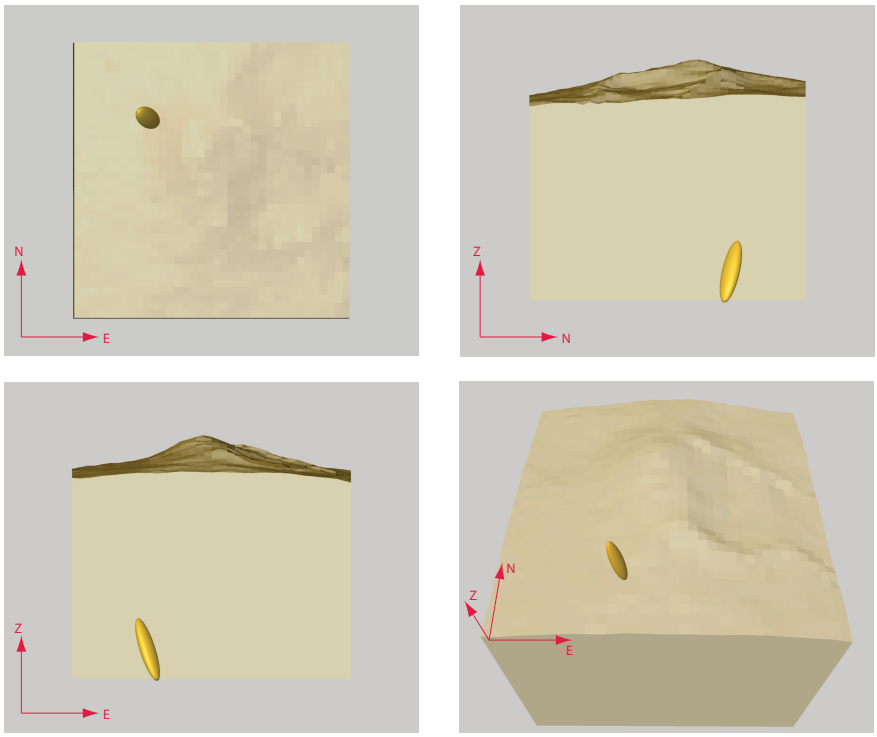

Figure 10. Representation of the ellipsoid within the medium. All the inversions retrieve an ellipsoid dipping SE and located under the NW flank of Mt. Etna. The axes ratios are approximately c/a = 0.2 and b/a = 0.3.